UNIVERSITY OF TARTU
Faculty of Science and Technology
Institute of Technology

Pavels Kapitulskis

Cobalt, iron, and nitrogen co-doped graphene coated ceramic nanowire-based bifunctional oxygen electrocatalyst for Zn-air battery

Bachelor's Thesis (12 ECTS)

Curriculum Science and Technology

Supervisor(s):
Professor, PhD Kaido Tammeveski
Research fellow, PhD Marek Mooste

Tartu 2023

Cobalt, iron, and nitrogen co-doped graphene coated ceramic nanowire-based bifunctional oxygen electrocatalyst for Zn-air battery

Abstract:

Structural and elemental composition of several graphene-coated Al_2O_3 nanowire-based catalyst materials prepared by functionalization with dicyandiamide and Fe and Co salts via pyrolysis were studied using several physical characterisation methods. Electrocatalytic oxygen reduction reaction (ORR) activity of the materials was studied using the rotating disk electrode method in a 0.1 M KOH solution. Using the same method, the oxygen evolution reaction activity was studied for the catalyst material with the highest ORR activity. Additionally, the catalyst's rechargeable Zn-air battery performance was assessed, showing superior power output and cycle life than those of a commercial Pt-Ru/C catalyst.

Keywords: electrocatalysis, oxygen reduction reaction, oxygen evolution reaction, non-precious metal catalyst, Zn-air battery, ceramic nanowire

CERCS: P401 Electrochemistry

Co, Fe ja N kaasdopeeritud grafeeniga kaetud keraamilistel nanotraatidel põhinev bifunktsionaalne hapniku elektrokatalüsaator Zn-õhk akule

Lühikokkuvõte:

Töös uuriti grafeeniga kaetud Al_2O_3 nanotraatidel põhinevate katalüsaatorite struktuurset ja elemendilist koostist. Katalüsaatormaterjalid valmistati ditsüandiamiidi ja Fe ning Co sooli kasutades pürolüüsi meetodil ja neid uuriti mitme füüsikalise karakteriseerimise meetodiga. Materjalide hapniku redutseerimisreaktsiooni aktiivsust uuriti 0,1 M KOH lahuses pöörleva ketaselektroodi meetodil. Sama meetodit kasutades uuriti ka hapniku eraldumisreaktsiooni aktiivsust kõrgeima hapniku redutseerumise aktiivsusega materjali puhul. Lisaks uuriti seda katalüsaatorit Zn-õhk patarei ja aku õhuelektroodil, mis näitas kõrgeimat maksimaalset võimsust ja laadimis-tühjenemise tsüklite eluiga võrreldes Pt-Ru/C katalüsaatoriga.

Võtmesõnad: elektrokatalüüs, hapniku redutseerimise reaktsioon, hapniku eraldumise reaktsioon, mitteväärismetallkatalüsaator, tsink-õhk aku, keraamiline nanotraat

CERCS: P401 Elektrokeemia

TABLE OF CONTENTS

ABBREVIATIONS

AEMFC	Anion exchange membrane fuel cell
CV	Cyclic voltammetry
CVD	Chemical vapour deposition
DCDA	Dicyandiamide
EDX	Energy-dispersive X-ray spectroscopy
GC	Glassy carbon
GDL	Gas diffusion layer
GR-NW	Graphene-coated Al_2O_3 nanowire
K-L	Koutecky-Levich
MNP	Metallic nanoparticles
NPMC	Non-precious metal catalyst
OER	Oxygen evolution reaction
ORR	Oxygen reduction reaction
PGM	Platinum-group metal
RDE	Rotating disk electrode
RHE	Reversible hydrogen electrode
RZAB	Rechargeable zinc-air battery
SCE	Saturated calomel electrode
SEM	Scanning electron microscopy
STEM	Scanning transmission electron microscopy
TEM	Transmission electron microscopy
TM	Transition metal
XPS	X-ray photoelectron spectroscopy
ZAB	Zinc-air battery

INTRODUCTION

Over the past few decades, demand for environmentally sustainable energy production and conversion has increased. Together with rising use of renewable energy, the need for high-capacity energy storage has become apparent. Rechargeable Zn-air battery (RZAB) is one of the most promising type of energy storage device, owing to the readily available materials, high energy density, low cost, and safety [1]. The oxygen reduction reaction (ORR) and its inverse reaction, the oxygen evolution reaction (OER), are the key processes taking place at the air-electrode of a RZAB. Both reactions possess slow kinetics, so a bifunctional ORR/OER catalyst is a necessity for a RZAB to produce sufficient power and recharge efficiently [2].

So far, Pt-group metals (PGM) and their oxides have been the most suitable catalysts for RZABs, due to their high ORR and OER activity, correspondingly. This has limited the use of RZABs, owing to the high cost of Pt-group metals and their limited availability. Many researchers have focused on designing alternative catalysts which do not contain precious metals, but still possess high electrocatalytic activity towards both ORR and OER. It has been established that transition metal and nitrogen co-doped high surface area nanocarbon catalysts are the most promising alternatives to replace PGM-containing ones [3, 4].

The most important features of bifunctional ORR/OER carbon-based catalysts are their high surface area and high electrical conductivity; however, these two properties could get in conflict. A higher surface area could correspond to a more amorphous structure, which in turn could mean higher electrical resistance. One way to circumvent this is to deposit carbon onto a substrate material with a high surface area, such that a thin layer of highly conductive sp^2-hybridized carbon is formed. Therefore, it has been presumed that graphene-coated Al_2O_3 nanowire could serve as a basis for an efficient ORR/OER bifunctional catalyst. In addition, this material has already been employed successfully as a support material for PGM-based catalysts for ORR in an acidic medium [5].

In the present work, graphene-coated Al_2O_3 nanowires were used as the support material for non-precious metal bifunctional electrocatalysts for oxygen electrode reactions through functionalization with N, Fe and Co active centres via high-temperature pyrolysis in N_2 atmosphere. The resulting material was studied as an ORR and OER electrocatalyst by rotating disk electrode method, and as an air-electrode catalyst for primary and secondary ZAB.

1 LITERATURE REVIEW

1.1 Zn-air battery

In the last decade, interest in Zn-air batteries (ZAB) has increased significantly [1]. In a primary ZAB electrical energy is extracted through oxidation of metallic zinc and reduction of atmospheric oxygen. In a ZAB with an alkaline electrolyte (Scheme 1), at the cathode atmospheric oxygen is reduced to OH^- ions with help of an air-electrode catalyst, while at the anode OH^- ions oxidize metallic zinc into ZnO. The difference in the electrical potentials of the anode and cathode half-reactions creates an electromotive force across the contacts of the battery, allowing for current generation.

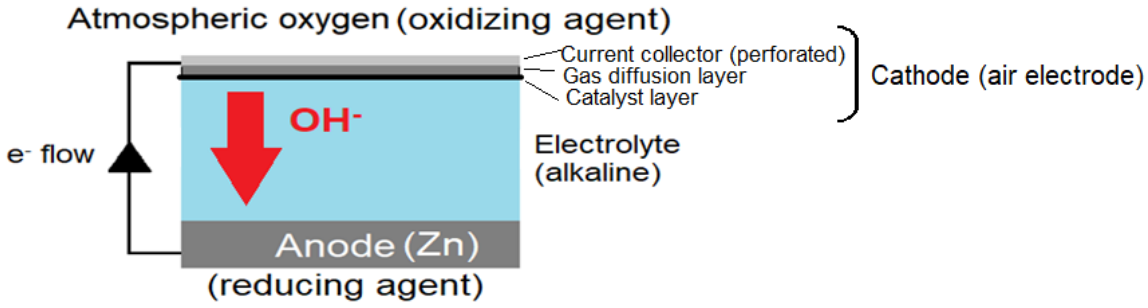

Scheme 1. Working principle of a primary Zn-air battery with an alkaline electrolyte.

Metal-air batteries, and especially ZAB, gained recognition as a high-capacity, cheap, safe, and sustainable energy storage option. Primary (i.e. non-rechargeable) ZABs have been known since the late 19th century, and commercially used since 1932 for low-power long-duration applications. Despite being a subject of study since the early 1960s [6], electrically rechargeable zinc-air cells (i.e. secondary ZAB or RZAB) have rarely been used in practice until recently due to multiple limitations, the most significant of which are low output power and poor cycle life [7, 8].

Today, the usage of ZABs is still limited, but is expected to grow significantly in the coming years [7]. ZABs, both primary and secondary, have been extensively studied as a method for electric vehicle propulsion, and RZABs are used commercially for grid energy storage (e.g. Eos Energy Enterprises Inc.).

The performance of a RZAB hinges on the rate of the oxygen reduction reaction (ORR) and the oxygen evolution reaction (OER). The two reactions taking place at the air-electrode are inverses of each other: ORR proceeds while discharging, and OER occurs during charging. While ORR occurs at the air-electrode cathode, the metallic Zn electrode as anode is partially

dissolved and replaced by ZnO. During anodic reaction of OER at the air-electrode, the layer of ZnO is dissolved at the Zn electrode (cathode), and metallic Zn is deposited. An ideal catalyst would have high bifunctional activity to achieve high performance for both, charging and discharging. The excellent ORR activity belongs to PGM catalysts, while the PGM oxides possess high OER activity. Both types of catalyst have poor bifunctionality [9] and must be combined at the air-electrode for sufficient RZAB performance (for example, a mix of Pt/C and RuO_2 [10]). In addition, the scarcity of PGMs make ZABs with such catalysts both commercially and environmentally unfeasible.

1.2 Oxygen reduction and evolution reactions

The electrocatalytic activity towards the ORR and OER of the air-electrode catalyst material defines the performance of the ZAB. During oxygen reduction, electrons are transferred to oxygen molecules adsorbed on the surface of the cathode. The oxygen is reduced according to one of two pathways, depending on properties of catalyst and electrolyte:

1. Direct $4e^-$ pathway:

   $$O_2 + 2H_2O + 4e^- \rightarrow 4OH^- \quad (1)$$

2. Series pathway:

   $$O_2 + H_2O + 2e^- \rightarrow HO_2^- + OH^- \quad (2)$$

   $$HO_2^- + H_2O + 2e^- \rightarrow 3OH^- \quad (3)$$

It is important to note that the above reactions (1-3) occur as described only in alkaline media. Variants for acidic environments exist, but are outside the scope of this study.

Intermediate HO_2^- anions are highly corrosive and reduce the lifetime of the system, which is why the direct $4e^-$ ORR pathway is preferred. Along with increased stability, the lack of intermediates allows for higher current efficiency and operating voltage [9].

Oxygen reduction is by far the slowest reaction in the ZAB system during discharging, due to the high bond energy of the oxygen molecule. It has been shown that the ORR activity of a metal catalyst varies depending on oxygen binding energy, with the best results achieved by PGMs [9, 11]. Because of this, currently the most used catalyst for these reactions is Pt, which significantly raises the price of both materials and manufacturing. Additionally, as mentioned before, Pt-based catalysts have low bifunctionality, meaning the cells that use them recharge slowly and inefficiently, if at all.

Oxygen evolution is a more complex set of reactions where molecular oxygen is produced at the air-electrode anode, while at the cathode Zn cycles between its metallic form and various oxygen-containing intermediates [9]. The combined result for all of these reactions at the air-electrode anode yields a mechanism equivalent to ORR in the reverse reaction [12]:

$$4OH^- \rightarrow O_2 + 2H_2O + 4e^- \quad (4)$$

1.3 Co, Fe, and N co-doped nanocarbon catalysts for ORR and OER

Non-precious metal catalysts (NPMCs) are a crucial development for practically viable ZABs. While being cheaper than PGM catalysts, they can possess equal or even higher bifunctional ORR/OER activity, making the cells that use them charge and discharge faster and with less energy loss. The most studied NPMCs are, in general, composed of nanocarbon materials doped with nitrogen and transition metals [3]. In brief, a suspension of nanocarbon support and the precursors for desired transition metal and N dopants is created, afterwards it is dried and the solid residue undergoes high-temperature pyrolysis (e.g. at 800 °C). This process creates a doped highly porous nanocarbon material, which can possess beneficial catalytic properties for both oxygen reactions contributed by the high specific surface area. Also, due to the high conductivity of structured carbon (specifically, C in sp^2 hybridization), the transfer of charge within the catalyst is accelerated and catalytic properties are enhanced.

Due to the high electronegativity, N atoms induce a positive charge on the C atoms around them in carbon material, which increases O_2 adsorption and therefore helps to catalyse the ORR. In addition, transition metal atoms form complexes, coordinating with several nitrogen atoms (M-N_x). These M-N_x centres (e.g. Fe-N_x) can promote a direct $4e^-$ oxygen reduction pathway and increase catalytic activity [3]. It has been shown that nitrogen defects catalyse OER as well as ORR, depending on the type of bond formed between the nitrogen atom and carbon substrate [9].

Liu et al. [13] reported in 2010 that metal-free N-doped graphitic carbon can possess better ORR catalytic properties in alkaline environment than commercially available Pt/C catalyst. In addition, in 2014 Liang et al. [14] found that high porosity is beneficial for electrocatalytic properties. It has been further determined that graphitic-N defects control the ORR activity, while pyridinic-N defects control the OER activity in the case of (transition) metal-free NPMCs [9]. The effects of incorporating transition metal dopants have been known since 1964 from the pioneering work of Jasinski [15], and in the late 1970s it was found that high-

temperature pyrolysis greatly improves both stability and ORR activity of NPMCs [16]. In 1989, it was discovered that M-N_x clusters can form spontaneously from metal and nitrogen precursors and do not need to be present originally in M-N_x form, allowing the use of easily accessible and cheap materials [17]. In several investigations, the Fe-N_x and Co-N_x species have been found to exhibit the highest ORR activity among different M-N_x materials, with half-wave potential ($E_{1/2}$) approaching that of commercial PGM catalysts. N-doped carbon with Fe/Co co-doping exhibits $E_{1/2}$ only 20 mV lower than that of a Pt/C catalyst [3, 18, 19].

It was shown by Sokka et al. [20] using electrospun carbon nanofiber NPMCs that harsher acid-leaching conditions correlate with higher $E_{1/2}$ values, better ORR/OER reversibility (ΔE) and lower OER potential (potential at 10 mA cm^{-2}, $E_{j=10}$) values. Acid-leached materials showed $E_{1/2}$, ΔE, and $E_{j=10}$ values of -0.15 V, 0.65 V, and 0.80 V (vs. saturated calomel electrode (SCE)), respectively, while the same potentials for untreated materials were measured at -0.19 V, 0.71 V, and 0.90 V (vs. SCE), respectively. It is worth noting, however, that the same correlation also applies to the catalyst's S content, which was introduced due to the acid treatment. Additionally, the study showed that using two transition metals (TM) shows significantly higher $E_{1/2}$ values compared to single TM NPMCs, with the highest single-TM $E_{1/2}$ measured to be only -0.19 V (vs. SCE). Using optimised carbon nanofiber materials, it was possible to achieve anion exchange membrane fuel cell (AEMFC) power output at 0.65 V only 11% lower than that of commercial Pt/C cathode catalyst. In addition, Kumar et al. [21] achieved AEMFC power densities of over 500 mW cm^{-2}, with $E_{1/2}$, ΔE, and $E_{j=10}$ values of -0.15 V, 0.77 V, and 0.62 V (vs. SCE) correspondingly in 0.1 M KOH electrolyte, using two TM-containing N-doped multiwalled carbon nanotube-based catalysts.

Bezerra et al. and Kumar et al. [22, 23] prepared NPMCs based on graphene-like carbon structures. Kumar et al. used multiwalled carbon nanotubes, while Bezerra et al. employed N-doped graphene nanoribbons derived from multiwalled carbon nanotubes. The works showed that carbon-based NPMCs possess better stability than traditional PGM catalysts. When used in a RZAB setup, the N-doped graphene nanoribbon catalyst cycled for over 20 hours before failure, and as a primary ZAB reached a maximum power density of 65 mW cm^{-2}, and the specific capacity of the ZAB was determined to be 686 mAh g_{Zn}^{-1}. In the same study, a Pt-Ru/C air-electrode catalyst RZAB failed after only 6 hours of testing. Although, as a primary ZAB with Pt-Ru/C reached a maximum power density of 81 mWcm^{-2}, with a specific capacity of 707 mAh g_{Zn}^{-1} [22]. The multiwalled carbon nanotube Fe/Ni catalyst cycled in RZAB configuration stably for over 48 hours using 1 mA cm^{-2}, while reaching a

maximum power density of 85 mW cm^{-2} as a primary ZAB, which is a higher power density than a Pt-Ru/C catalyst. Primary ZAB testing of full discharge at constant current was not performed in the latter study, so specific capacity was not determined [23]. Such remarkable catalytic performance was achieved through a simple mixing of Fe and Co phthalocyanines with multiwalled carbon nanotubes in suspension, followed by drying and pyrolysis.

Many other routes of producing NPMCs for ZAB air-electrode application have been also explored. Go et al. and Wu et al. [10, 24] experimented with inducing porosity controlled by condensing material onto sacrificial spheres, which would decompose during pyrolysis. Go et al. condensed Co/Fe impregnated polydopamine onto melamine-formaldehyde spheres, then pyrolysis was used to carbonize the polydopamine and decompose the sacrificial spheres. Wu et al. used Zn/Co metal-organic nanocrystals, which were also coated with Fe-impregnated polydopamine, and decomposed during pyrolysis. Sun et al. [25] enhanced electrical conductivity by introducing nanofiber filaments through electrospinning the precursor solution before pyrolysis. Wang et al. [26] used a C_3N_4 nanosheet structure to increase graphitic-N content. Zhang et al. [27] added separately prepared Fe/Co alloy nanoparticles coated with N-doped carbon to a basic Fe/Co carbonate, and determined that the presence of N-doped carbon coated Fe/Co alloy nanoparticles in the catalyst significantly improves stability and bifunctional activity. Wang et al. [28] showed that the use of an ionic liquid promotes dispersion of Fe/Co ions in precursors, and the formation of N-doped carbon coated Fe/Co alloy nanoparticles during pyrolysis.

Kumar et al. used multiwalled carbon nanotubes as the support material [29], which was modified by various bimetal phthalocyanines (TM = Mn, Ni, Co). After high-temperature pyrolysis these materials were active electrocatalysts for both the ORR and OER in alkaline media and showed also excellent ZAB performance with open circuit voltage of 1.338 V.

The Al_2O_3-based graphene-coated ceramic nanowire (GR-NW) catalyst support route used in this thesis is a novel method that has not been used before for the preparation of NPMC materials. The ORR/OER half-cell and ZAB results obtained for GR-NW-based catalysts in the present work can be compared to the ones of similar NPMC materials that were briefly described with their most important findings in previous paragraphs [10, 23-28].

2 THE AIMS OF THE THESIS

- Study the ORR and OER activity of GR-NW catalysts in an alkaline environment
- Analyse the surface and elemental content of GR-NW catalysts
- Measure primary and rechargeable ZAB performance of the best GR-NW catalyst
- Assess the suitability the best GR-NW catalyst for ZAB air-electrode application

3 EXPERIMENTAL

3.1 Preparation of catalyst materials

3.1.1 Preparation of graphene coated ceramic nanowires

Ceramic nanowires of Al_2O_3 were prepared *via* controlled oxidation of molten aluminium. Chemical vapor deposition (CVD) of carbon onto the ceramic nanowires was carried out at Tallinn University of Technology by Dr. Roman Ivanov [30]. The CVD setup is shown in Scheme 2. A sample of Al_2O_3 nanowire was placed in a quartz tube. It was heated in air to 1000 °C for 3 min in order to dry. After drying in air, the sample was taken out, weighed, and placed back into the tube. Argon was pumped into the tube at 1000 cm^3 min^{-1} and the sample was again dried at 1000 °C for 2 min. After the argon drying, CH_4 was pumped into the tube for 20 min at 200 cm^3 min^{-1} while maintaining 1000 °C. The CH_4 was evacuated using argon before cooling down. The cooled sample was taken out and weighed. The weight after air drying was 0.1034 g, and the final weight was 0.1783 g. In total 74.9 mg of carbon was deposited onto the Al_2O_3 ceramic nanowires, which were designated as GR-NW.

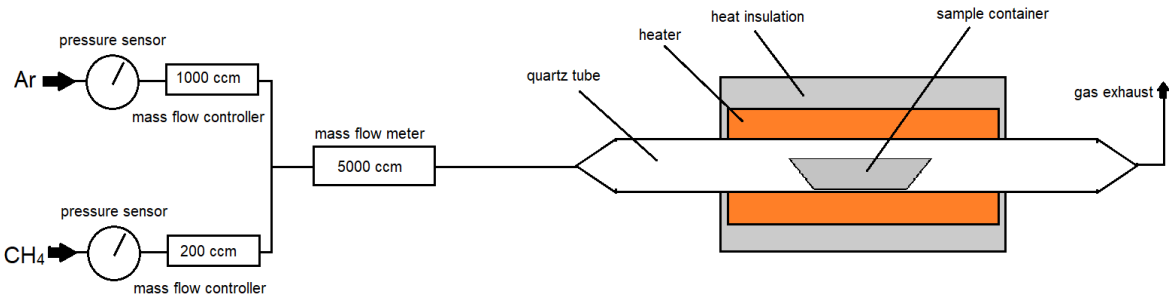

Scheme 2. Diagram of the setup used for CVD to prepare GR-NW material [30]

3.1.2 Functionalisation with N, Fe and Co

Nitrogen, Fe, and Co co-doping was achieved using methods reported by Ratso et al. [31]. Three different samples were prepared (GR-NW-N, GR-NW-N/Fe, GR-NW-N/Fe/Co).

To prepare GR-NW-N, 30 mg of GR-NW was placed into approx. 20 ml of ethanol, and the mixture was treated in an ultrasonic bath (Branson 1510E-MTH, Bransonic) for 30 min to create a suspension. 0.6 g of dicyandiamide (DCDA, Sigma-Aldrich, 99%) was added into the suspension, after which it was further sonicated for 2 more hours. The resulting suspension was transferred to a Petri dish and was left to dry overnight at 60 °C. After drying, the weight of the solid residue was measured at 622.4 mg. A pyrolysis setup according to an

earlier study [31] was used. The quartz tube, while open to air, was cleaned by ramping up to 1000 °C at 50 °C min^{-1}, followed by 7 min of dwell time. After the tube had cooled, the material was placed inside, and the tube was evacuated with N_2 gas. Under flowing N_2, the sample was heated to 800 °C with a ramping rate of 10 °C min^{-1}. After reaching 800 °C, constant temperature was maintained for 2 h, after which the system was left to cool down. At a temperature of approx. 100 °C the nitrogen flow was stopped, and the sample was taken out. After pyrolysis has finished, the final mass of the product was measured at 24.32 mg.

To prepare GR-NW-N/Fe catalyst, the same initial steps were followed as for GR-NW-N preparation. After adding DCDA, sonication was paused after 15 min. 2.5 mg of $FeCl_3$ (Sigma-Aldrich, 97%) was added into the suspension, after which sonication resumed for 2 h, followed by overnight drying at 60 °C. Mass of dry material was measured at 654 mg. An identical pyrolysis procedure as for GR-NW-N was carried out, after which the final sample weighed 28.7 mg.

During the preparation of GR-NW-N/Fe/Co catalyst, 20.7 mg of GR-NW was used. After creating an ethanol suspension, 0.42 g of DCDA was added, and after 15 min of sonication, 1.75 mg of $FeCl_3$ (Sigma-Aldrich, 97%) and 3.7 mg of $Co(CH_3COO)_2$ (Alfa Aesar, 98%) were added. The rest of the procedure matched exactly with the previous two materials. Dry mass before pyrolysis was measured at 449 mg, which was reduced to 17.63 mg after pyrolysis due to the carbonisation procedure.

3.2 Physical characterisation studies

Scanning electron microscopy (SEM) and transmission electron microscopy (TEM) studies were performed by Ms. Helle-Mai Piirsoo (MSc) at University of Tartu Institute of Physics. SEM was performed with Helios Nanolab 600 (FEI) which was equipped with INCA Energy 350 (Oxford Instruments) energy dispersive X-ray (EDX) analysis detector. EDX analysis were averaged over multiple measurements (scan area of 17 µm × 17 µm) along the surface of the material. The powdered sample was added to 2-propanol and the mixture was kept in an ultrasonic bath for about 5 min. The solution was dropped on a lacey mesh carbon-coated TEM grid, which was left to air dry for a day before TEM analysis. The TEM studies were performed with Titan Themis 200 (FEI) operating at 200 kV in scanning mode (STEM). Spatial distribution of elements was characterized with SuperX (Bruker) energy dispersive X-ray spectroscopy system in Titan Themis 200 microscope.

X-ray photoelectron spectroscopy (XPS) studies were performed by Dr. Arvo Kikas at the Institute of Physics of University of Tartu. XPS measurements were taken with a SCIENTA SES-100 spectrometer by using 200 eV pass energy. For excitation the non-monochromatic Mg Kα X–ray photons (energy 1253.6 eV) from X-ray source XRE2 were used. The electron take-off angle was 90º and the pressure inside the analysis chamber was below 10^{-9} Torr during the data collection. The raw data was processed using the CasaXPS software (version 2.3.17). Data processing involved removal of X-ray satellites, and peak fitting using the Gauss–Lorentz hybrid function and combination of linear and Shirley backgrounds.

Raman spectroscopy was performed by Dr. Aleksei Treštšalov at the Institute of Physics of University of Tartu. Micro-Raman spectra were recorded in the back-scattering geometry on an inVia Renishaw spectrometer in conjunction with confocal microscope (Leica Microsystems CMS GmbH), 50X objective and an argon ion laser operated at 514.5 nm. Low incident laser power density at the sample prevented excessive sample heating and/or decomposition, while allowing getting averaged information over ~200 μm^2 area in a single exposure.

3.3 Electrochemical studies

3.3.1 ORR and OER half-cell studies

A catalyst ink was prepared for each NPMC material. For each ink, 4 mg of NPMC material was sonicated for 1 h in a mixture of 495 µl milliQ pure water, 495 µl 2-propanol, and 5 µl Nafion® solution (5%, Sigma-Aldrich). A 5 µl drop of such ink was placed onto a glassy carbon (GC, geometric area 0.2 cm^2) electrode polished and cleaned according to previously reported procedure [32], which was then left to dry at 60 °C. Once dry, a second 5 µl drop was placed onto the electrode, which was again left to dry at 60 °C. This procedure resulted in a NPMC loading of 0.2 mg cm^{-2}. Pt-Ru/C (HiSPEC 12100, 50% Pt and 25% Ru; Alfa Aesar) catalyst coated GC electrode with the loading of 25 µg Pt, Ru cm^{-2} was prepared according to the procedure from a previous study [33]. The corresponding half-cell studies with Pt-Ru/C coated electrode were performed by Dr. Marek Mooste.

Electrochemical studies were carried out in an O_2-saturated (99.999%, Linde) solution of 0.1 M KOH (Sigma-Aldrich, purity ≥85%). A three-electrode system was used with catalyst-coated GC as a working electrode, saturated calomel electrode (SCE) as reference electrode, and Pt-wire as a counter electrode. The studies were performed with instruments used in previous work [20]. Cyclic voltammetry (CV) scanning with a rotating disk electrode (RDE)

was employed for the measurements. Polarization curves for ORR in the cathodic direction were recorded at rotation rates of 360, 610, 960, 1900, 3100, and 4600 rpm. Background current was measured in an Ar-saturated (99.999%, Linde) aqueous solution of 0.1 M KOH. In addition, OER polarization curves were recorded in the anodic direction at 1900 rpm in an Ar-saturated aqueous solution of 0.1 M KOH. The polarisation curves were compensated for iR-drop using ohmic resistance values obtained by the current interruption method. All of the electrochemical experiments were repeated at least three times to verify the reproducibility of the reported results.

3.3.2 ZAB setup and testing

An in-house built ZAB setup was constructed identical to the one used by Muuli et al. [34]. NPMC ink was prepared with 7 mg NPMC, 200 µl MilliQ water, 600 µl ethanol, and 20 µl Nafion® 5% solution, and was sonicated for 1.5 hours. 100 µl of NPMC ink was spread onto a 1.9 × 1.9 cm gas diffusion layer (GDL, *Sigracet BB39*), and was left to dry at 60 °C. This procedure was repeated for additional 7 times to ensure the desired NPMC final loading of 2 mg cm^{-2}. For comparison, the Pt-Ru/C catalyst with the loading of 1 mg cm^{-2} at the air-electrode was also employed, and the ZAB studies with Pt-Ru/C air-electrode catalyst were performed by Dr. Marek Mooste. On the air-electrode side, Ni mesh was placed over the air entrance as a current collector. NPMC coated GDL was placed between the mesh and electrolyte compartment, with NPMC coating facing towards the electrolyte. The catalyst layer area exposed to the electrolyte solution at the air-electrode of 0.79 cm^2 was outlined with acrylonitrile butadiene rubber O-ring. For the electrolyte, an aqueous solution of 6 M KOH + 0.2 M $Zn(CH_3COO)_2 \cdot 2H_2O$ (Fisher Scientific, 98%) was used. For the Zn electrode, 0.2 mm thick Zn foil (99.9%, Auto-plaza) was used. The area of the Zn foil electrode exposed to the electrolyte was 2.55 cm^2. Scheme 3 shows a simple diagram of the ZAB setup used.

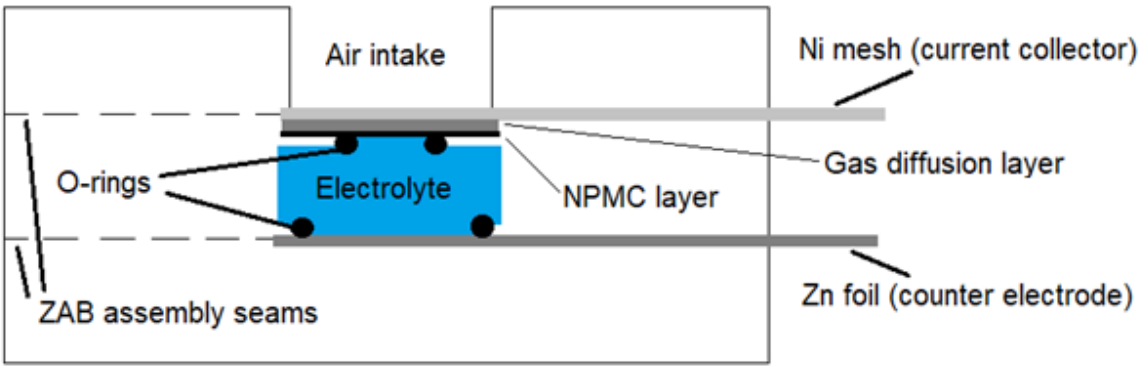

Scheme 3. Schematic representation of ZAB cell [34].

The power curve of the primary ZAB was recorded in galvanostatic mode with scan rates of 2 mA min^{-1} below 2 mA, and 10 mA min^{-1} between 2 mA and 300 mA. Additionally, the voltage during total discharge over time was measured in two separate total discharge runs with freshly prepared setups using a current of 16 mA. Before and after each total discharge run, the Zn anode was weighed to determine specific capacity of the ZAB. Both types of primary ZAB tests were stopped when the voltage of the cell dropped below 0.2 V.

The secondary ZAB was set to continuous charge-discharge cycling. For every cycle, 4 mA was applied to the RZAB for 300 s, followed by -4 mA for another 300 s. This procedure was repeated until failure of the ZAB due to ZnO layer formation [33]. 4 cycling runs were recorded to investigate long-time operation of the cell. Prior to every new run, the electrolyte and Zn foil were changed to fresh ones. The current values reported for primary and secondary ZAB experiments have been converted to current density (mA cm^{-2}) using the active geometric area of the air-electrode (0.79 cm^2).

4 RESULTS AND DISCUSSION

4.1 Physical characterisation of the materials

Fig. 1 shows the SEM images of GR-NW-N, GR-NW-N/Fe, and GR-NW-N/Fe/Co catalysts. All three materials have a similar structure, consisting of approx. 15 nm diameter fibres (Figs. 1c, 1f, 1i). This is to be expected, as all catalyst materials were created from the same sample of original GR-NW. In the case of GR-NW-N/Fe/Co, there could be metallic nano-particles (MNP) present, ranging in size from 15 nm to 40 nm. Although, the presence of MNP cannot be stated using only the SEM results and further characterisation is needed. The overall structure of the GR-NW-based catalysts is similar to that of Pt-nanoparticle coated GR-NW created by Hussain et al. [5], where GR-NW material of the same origin was used.

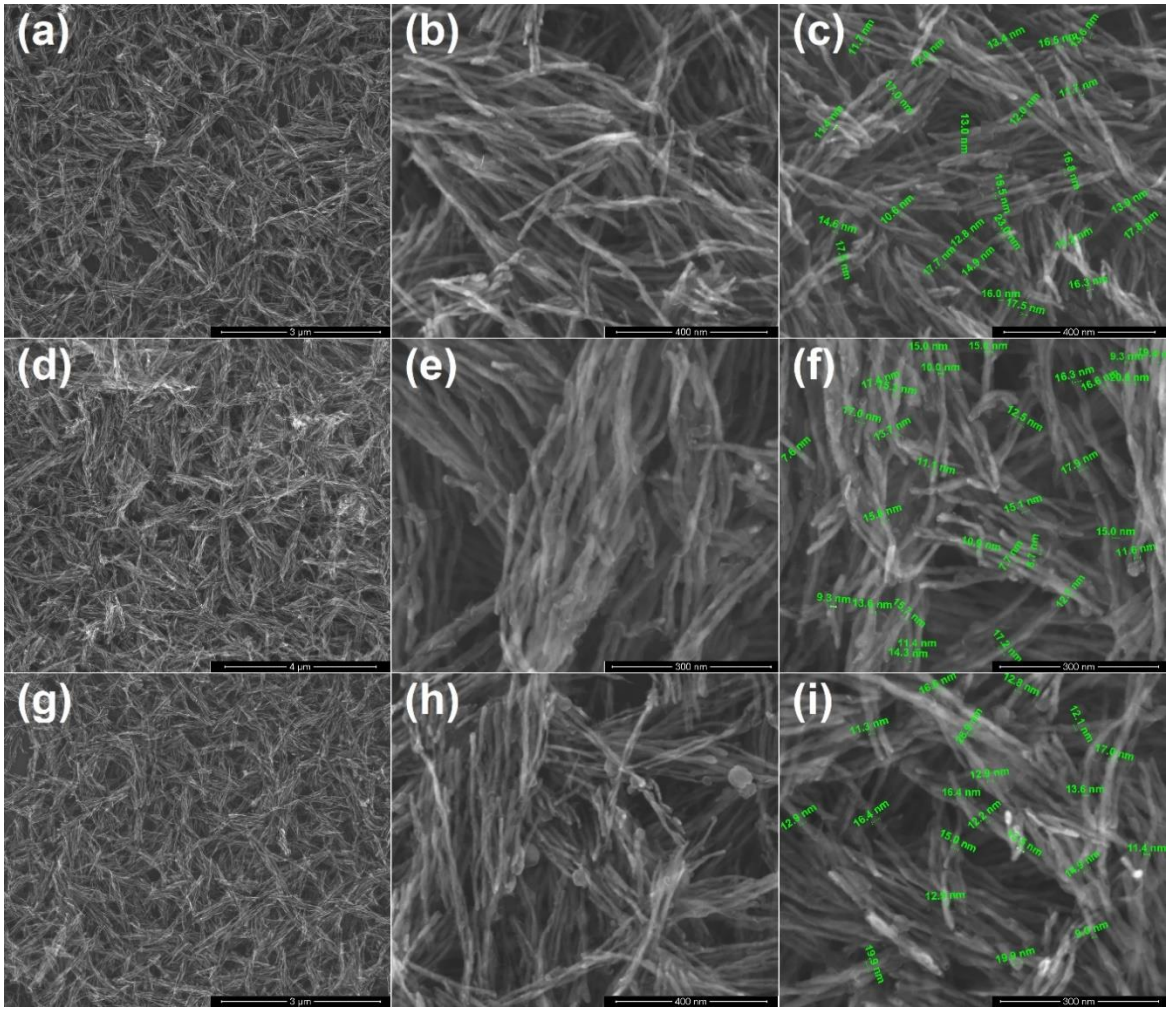

Figure 1. Scanning electron microscopy images of (a-c) GR-NW-N, (d-f) GR-NW-N/Fe, (g-i) GR-NW-N/Fe/Co with different magnification, (c, f, i) with labelled nanofiber size.

SEM-EDX was used to determine the elemental composition of the catalyst material (Table 1). Nitrogen could not be distinguished from the EDX spectrum, as its amount was too low to be detected by this method. In more specific, the signal was lost in the noise, or the peak overlapping of different elements masked the peak of N. Therefore, further characterisation is needed to detect the presence and amount of nitrogen.

Table 1. Elemental composition (wt%) of catalyst materials, measured using SEM-EDX.

Catalyst material	**C**	**N**	**O**	**Al**	**Fe**	**Co**
GR-NW-N	43.4	0	32.4	24.2	0	0
GR-NW-N/Fe	40.5	0	31.0	25.8	2.7	0
GR-NW-N/Fe/Co	41.6	0	33.5	21.8	0.8	2.3

The weight ratio of Al to O is close to a 1:2 molar ratio, rather than the 2:3 molar ratio seen in Al_2O_3, suggesting that oxidation of the material could have occurred. Additionally, for GR-NW-N/Fe/Co, the weight ratio of Fe and Co in the precursor ingredients was approx. 1:2, while in the final material their ratio is close to 1:3. Surprisingly, the fraction of Fe has also decreased significantly from GR-NW-N/Fe to GR-NW-N/Fe/Co, despite both materials having the same ratio of Fe to GR-NW in the precursors.

The proposed presence of MNP seen in GR-NW-N/Fe/Co material (Figs. 1h, 1i) were further examined using TEM (Fig. 2 and Fig. S1 in Appendix). Herein, the presence of nitrogen was also detected, and a uniform distribution of N and O was detected throughout the material. Meanwhile, both Fe and Co appear to be present irregularly and more densely in spherical formations indicating the presence of MNP. Both Fe and Co seem to be evenly distributed in the nanoparticles. This suggests that the transition metals are well mixed, and the nanoparticles mostly consist of a Fe/Co alloy. This would agree with the findings of Kim et al. [35] who has also evidenced Fe/Co alloy MNPs in nanocarbon catalysts using TEM. Due to the detection of oxygen, transition metal oxides could also be present. Furthermore, the co-existence of N and transition metals could indicate to the presence of FeN_x/CoN_x groups, but their detection would need additional confirmation with a different method (e.g. XPS).

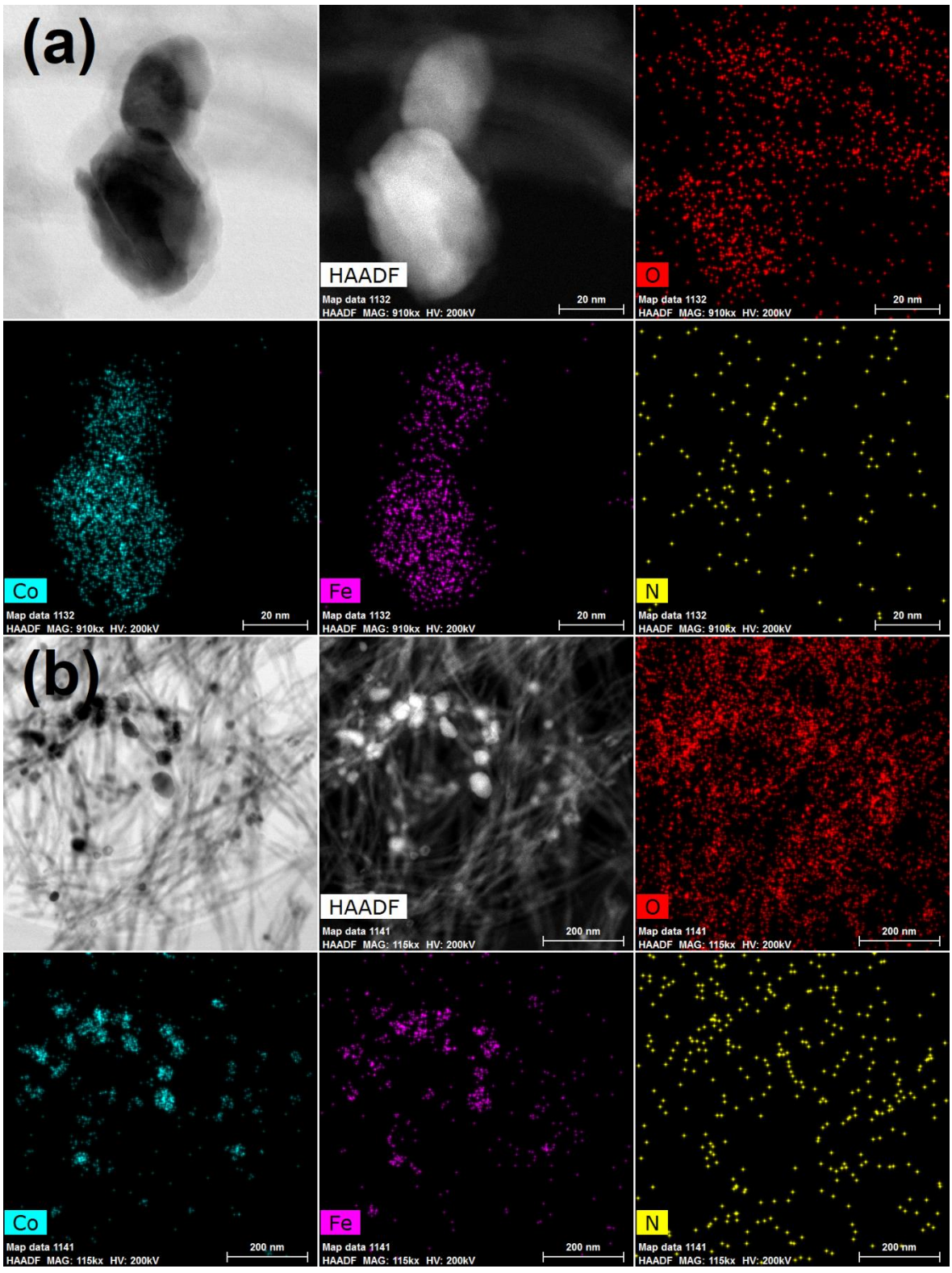

Figure 2. Bright-field and high-angle annular dark field (HAADF) STEM images of GR-NW-N/Fe/Co at two different magnifications and corresponding EDX elemental maps of oxygen, cobalt, iron, and nitrogen.

The elemental composition of GR-NW-N/Fe and GR-NW-N/Fe/Co was examined further with XPS (Table 2, Figs. 3, 4). The survey spectra of both materials show large peaks of Al

and O. As expected, Al only has one peak belonging to Al_2O_3 (Figs. 3b, 4b), however O contributes a multitude of pronounced C-O peaks (Figs. 3e, 4e), confirming that quite significant oxidation of the material had occurred. Based on the observation in Fig. 2, it is clear that almost all of the added oxygen could be bound to carbon. Partially, due to this oxidation, only around 50% of surface carbon is in sp^2 form, with a large fraction of C being bound to different functionalities. Interestingly, metallic Fe(0) was not detected in GR-NW-N/Fe/Co (Fig. 4f), but was found in GR-NW-N/Fe (Fig 3f). This indicates that the signal of Fe(0) could be masked by the high background noise in the XPS spectrum. The measured atomic ratio of Fe and Co in GR-NW-N/Fe/Co still corresponds to a 1:3 weight ratio and agrees with the SEM-EDX results, however unlike EDX, the fraction of Fe was measured as nearly identical in both materials. The difference between the SEM-EDX and XPS results can be explained by the greater analysis depth of SEM-EDX. If Fe is concentrated on the surface of the MNP, while Co is more evenly distributed throughout the entire volume, XPS would fail to detect Co deeper inside the material, and register a higher relative number of Fe atoms. Similarly, if there is an oxide layer on the surface of the MNP, XPS would fail to penetrate deeper into the material, and metallic TM species would have a reduced signal, or possibly would not be detected at all. This could be the explanation for the absence of Fe(0) signal in the high-resolution XPS spectrum registered for GR-NW-N/Fe/Co in Fig. 4f.

Table 2. Elemental composition (at%) of GR-NW-N/Fe and GR-NW-N/Fe/Co samples, and relative amounts (%) of nitrogen species (N1 – pyridinic-N, N2 – M-N_x, N3 – pyrrolic-N, N4 – graphitic-N, N5 – bulk N-H, N6 – imine), determined from the XPS data in Figs. 3, 4.

Catalyst	**C**	**N**	**O**	**Al**	**Fe**	**Co**
GR-NW-N/Fe	86.12	0.54	7.1	6.15	0.1	0
GR-NW-N/Fe/Co	83.46	0.41	8.99	6.58	0.13	0.42
Catalyst	**N1**	**N2**	**N3**	**N4**	**N5**	**N6**
GR-NW-N/Fe	42.6	18.5	18.5	5.6	3.7	11.1
GR-NW-N/Fe/Co	48.8	17.1	19.5	7.3	0	7.3

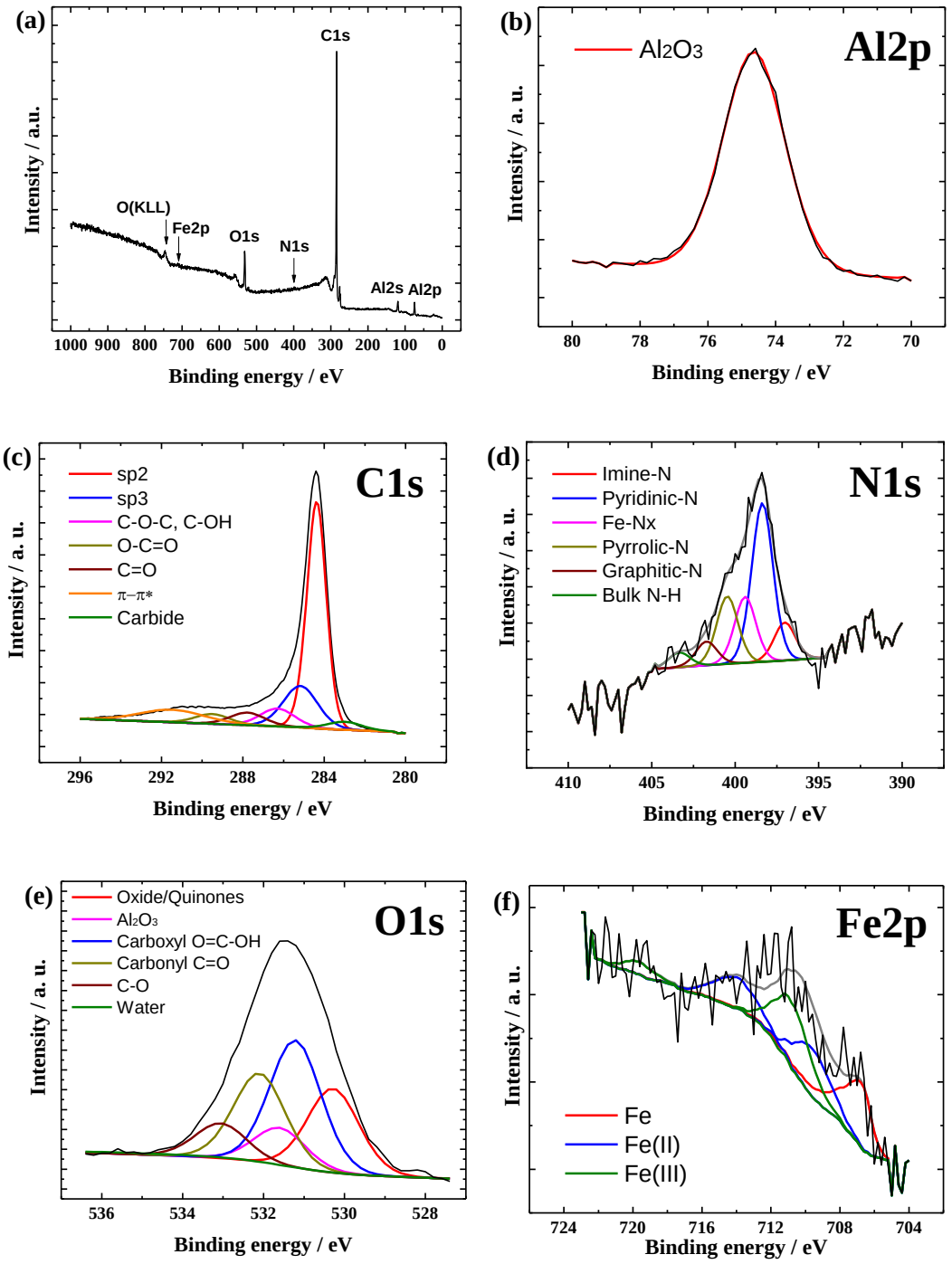

Figure 3. XPS spectra of GR-NW-N/Fe material coated on GC. (a) Survey spectrum and high-resolution XPS spectra in (b) Al2p, (c) C1s, (d) N1s, (e) O1s, and (f) Fe2p regions.

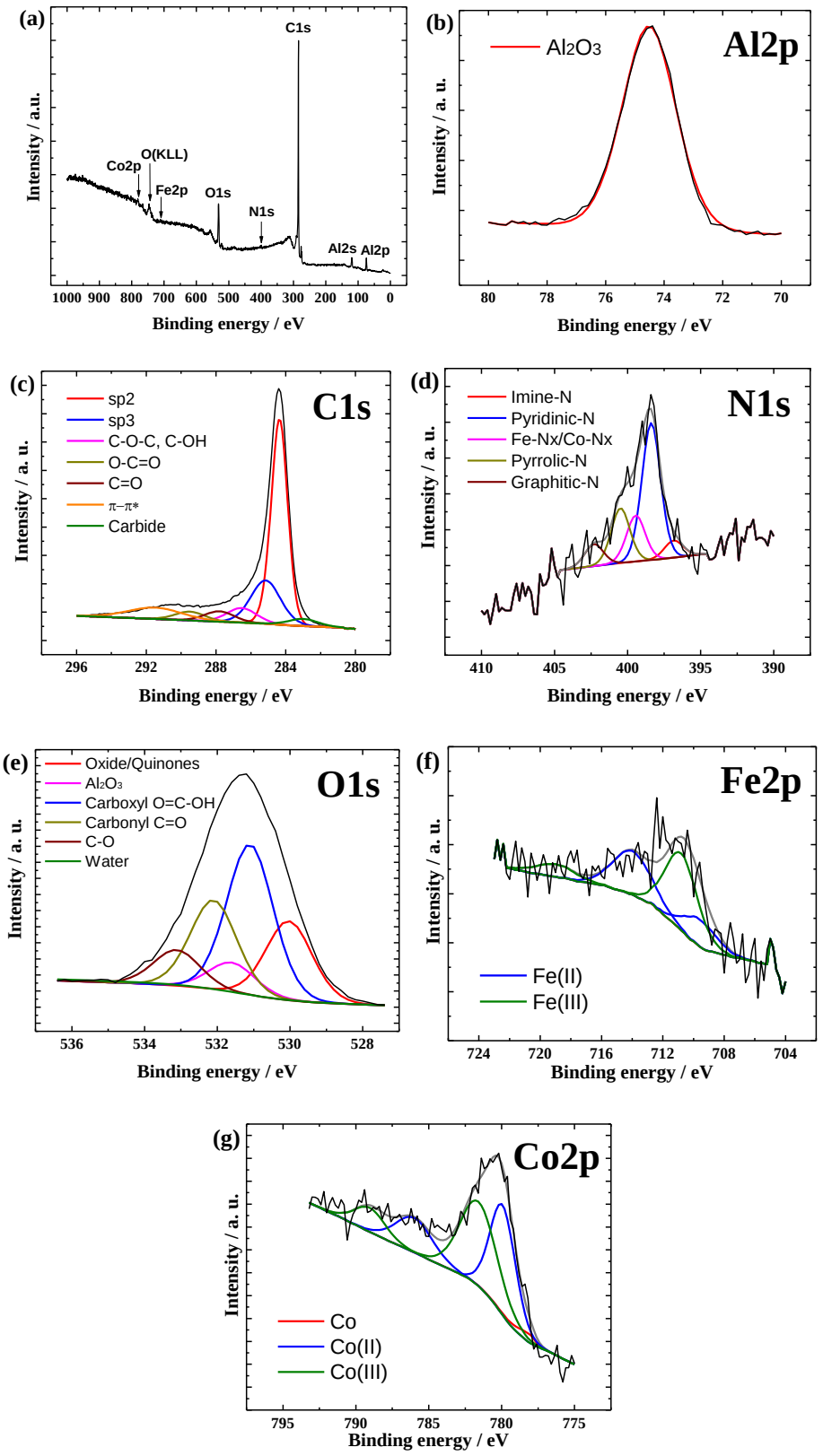

Figure 4. XPS spectra of GR-NW-N/Fe/Co material coated on GC. (a) Survey spectrum and high-resolution XPS spectra in (b) Al2p, (c) C1s, (d) N1s, (e) O1s, (f) Fe2p, and (g) Co2p regions.

Considering the characteristics of these two analysis methods (SEM-EDX vs. XPS), XPS results can be considered more important for OER and ORR electrocatalysis point of view, as these reactions occur mainly on the catalyst surface. Of the different species detected by XPS in the present work, M-N_x groups are highly active for ORR [18, 23]. Additionally, doped N species facilitate the ORR by increasing the limiting current density (graphitic-N) and increasing the onset potential (pyridinic-N and pyrrolic-N) [23]. Pyridinic-N has also been shown to possess OER activity [9]. TM oxides are considered very important for good OER performance [22, 23], and their presence could be evidenced by the detection of TMs in the oxidation states of (II) and (III).

The Raman spectra (Fig. 5) show a high similarity to that of carbon nanohorns from a study by Peña-Álvarez et al. [36]. The two peaks at around 1300 cm^{-1} and 1600 cm^{-1} correspond to the D and G bands, which can be used to describe graphene, and the collection of peaks in the 2400-3200 cm^{-1} region can be attributed to D-band overtones and combinations with D' and D" bands [36]. The D-band of a Raman spectrum is caused by defects (such as sp^3 carbon) in the sp^2 carbon atomic structure, and its intensity almost linearly depends on defect concentration. The G-band, on the other hand, corresponds to a vibration of carbon atoms within the plane of the graphene sheet consisting of sp^2 carbon framework. The intensity of the G-band is almost independent of the degree of functionalization, so the ratio of intensities of the D and G bands can be used to evaluate the degree of functionalization. It is worth noting that this method fails if the degree of functionalization is too high (>1 functional group per 100 carbon atoms), as both peaks begin to weaken due to loss of resonant properties [37]. The I_D/I_G ratios are close to 1.3 for all analysed materials, meaning that generally GR-NW graphene original structure has been well preserved after functionalization with N and TM species via high-temperature pyrolysis.

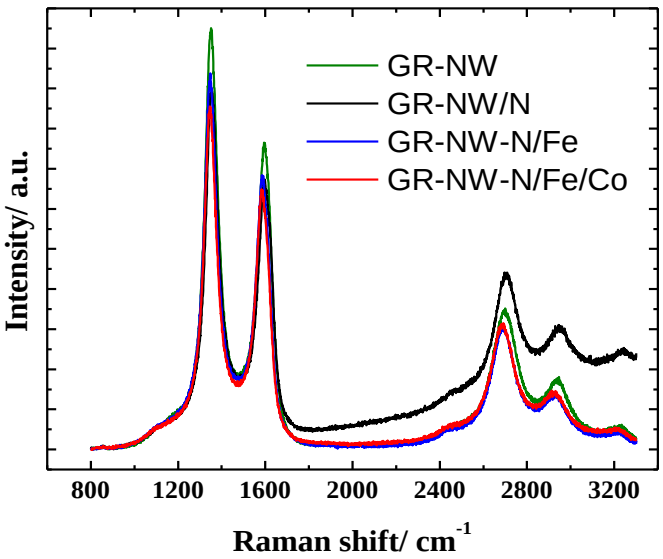

Figure 5. Raman spectra of GR-NW, GR-NW-N, GR-NW-N/Fe, and GR-NW-N/Fe/Co.

4.2 Oxygen reduction and evolution half-cell studies

RDE voltammetry curves at 1900 rpm were used to determine half-wave potential ($E_{1/2}$) and onset potential (E_{onset}) of the studied materials (Fig. 6, Table 3). Herein, E_{onset} is defined as the potential at which ORR current exceeds 0.02 mA (equal to 0.1 mA cm^{-2}). More positive $E_{1/2}$ and E_{onset} values suggest a better ORR performance of the catalyst. Simultaneously, a higher ORR current shows superiority of one material over another as an oxygen reduction catalyst. The original GR-NW is rather similar, or even better compared to GR-NW-N, as the introduction of only N-functionalities seems to negatively affect $E_{1/2}$, despite improving E_{onset} and limiting current. Both TM-containing materials show higher electrocatalytic ORR activity compared to GR-NW-N, as M-N_x functional groups are formed (Table 2, Figs. 3, 4) [18, 23]. GR-NW-N/Fe/Co shows by far the best ORR performance among the GR-NW-based catalyst materials and outperforms GR-NW-N/Fe, most likely due to the presence of Fe/Co alloy MNPs (Figs. 2 and S1) [27]. Compared to other similar catalysts reported in the literature (Table 3), the GR-NW-N/Fe/Co performance is rather moderate. Although, it should be noted that for the secondary ZAB application, the bifunctional activity of the catalyst is more important than only the ORR performance. Therefore, to assess the suitability of the material, the OER studies were also performed in addition to the ORR investigation.

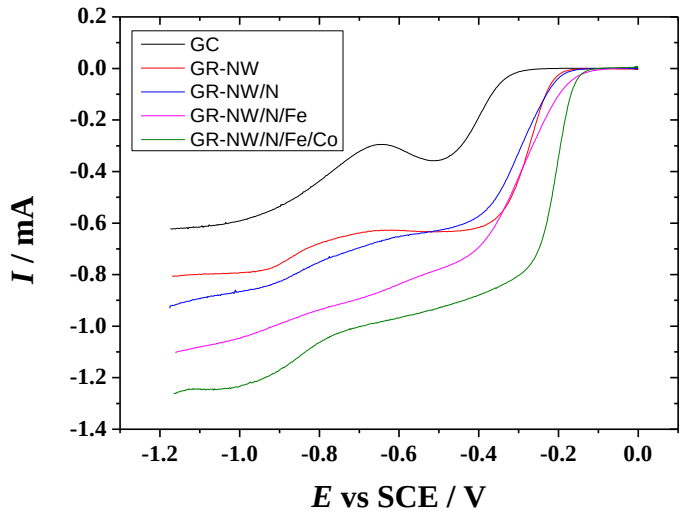

Figure 6. RDE voltammetry curves for oxygen reduction on catalyst-coated and bare GC electrodes in O_2-saturated 0.1 M KOH solution at 1900 rpm using a scan rate of 10 mV s^{-1}.

Table 3. Half-wave potential ($E_{1/2}$) and onset potential (E_{onset}) values of oxygen reduction for catalyst-coated and bare GC electrode in 0.1 M KOH at 1900 rpm (Fig. 6). The parameter values reported in other studies are given for comparison.

Catalyst	$E_{1/2}$, V	E_{onset}, V
GC	–	-0.31
GR-NW	-0.29	-0.20
GR-NW-N	-0.34	-0.18
GR-NW-N/Fe	-0.34	-0.14
GR-NW-N/Fe/Co	-0.23	-0.14
CoFe-N-OMC [18]	-0.17*	-0.01*
FeCoNCR-a [19]	-0.20*	-0.06*
Fe/Co/IL-CNF-800b [20]	-0.15	-0.04
FeCoN-MWNCT [21]	-0.15*	-0.08*

*Values converted to vs SCE using equation E(vs SCE) = E(vs RHE) - 0.241 - 0.059pH [33].

To find the number of electrons transferred per O_2 molecule, the Koutecky-Levich (K-L) analysis (Fig. 7) was also performed for bare GC, GR-NW, and GR-NW-N/Fe/Co electrodes at different rotation rates, according to the K-L equation [38, 39]:

$$\frac{1}{I} = \frac{1}{I_k} + \frac{1}{I_d} = -\frac{1}{nFAkc_{O_2}^b} - \frac{1}{0.62nFAD_{O_2}^{2/3}\nu^{-1/6}c_{O_2}^b\omega^{1/2}}$$

where n is the number of transferred electrons, I is the measured current, I_k and I_d are kinetic and diffusion-limited currents, k is the electrochemical rate constant for O_2 reduction, F is the Faraday constant (96485 C mol^{-1}), A is the geometric area of the electrode (0.2 cm^2), ω is the rotation rate, c^b is the concentration of oxygen in the bulk (1.2×10^{-6} mol cm^{-3} [38]), D is the diffusion coefficient of oxygen (1.9×10^{-5} cm^2 s^{-1} [38]) and ν is the kinematic viscosity of the electrolyte solution (0.01 cm^2 s^{-1} [38])

The calculated amount of electrons transferred for GC reaches 2.15, which agrees well with previously measured values [38]. The reason behind the n value for GC being higher than the expected n = 2, can be due to the technique used for polishing the electrodes. The value for GR-NW-N/Fe/Co is greater than 4, which can be attributed to an underestimation of the electrode surface area due to the fibrous structure of the coating material. The geometric surface area used for the K-L analysis assumes a perfectly smooth electrode surface, which is not the case with tested nanofibrous catalysts. This kind of error has been encountered also in previous studies [40]. Overall, GR-NW-N/Fe/Co catalyst seems to almost exclusively utilize the direct $4e^-$ ORR route according to Eq. (1), but series $2e^-$ pathway reactions by Eq. (2, 3) may still be occurring. GR-NW promotes the $2e^-$ ORR pathway by Eq. (2) at low overpotentials (> -0.9 V), and at high overpotentials also the direct $4e^-$ by Eq. (1) can occur. This shows that incorporation of transition metal and N dopants is highly effective increasing the ORR activity and reducing possible corrosion from peroxide, more so than incorporation of N-dopants alone. As expected, bare GC utilizes only the $2e^-$ pathway by Eq. (2) at all studied potentials.

GR-NW and GR-NW-N/Fe/Co show a mixed kinetic-diffusion control at higher potentials (more positive than -1.1 V), as linear extrapolations of the corresponding K-L plots have vertical intercepts greater than 0. However, both materials exhibited diffusion-limited ORR at potentials around -1.1 V, with a K-L line extrapolation intercept of zero. Overall, the GR-NW-N/Fe/Co material demonstrated the best ORR performance, and would be the most promising cathode catalyst for primary ZAB air-electrode application.

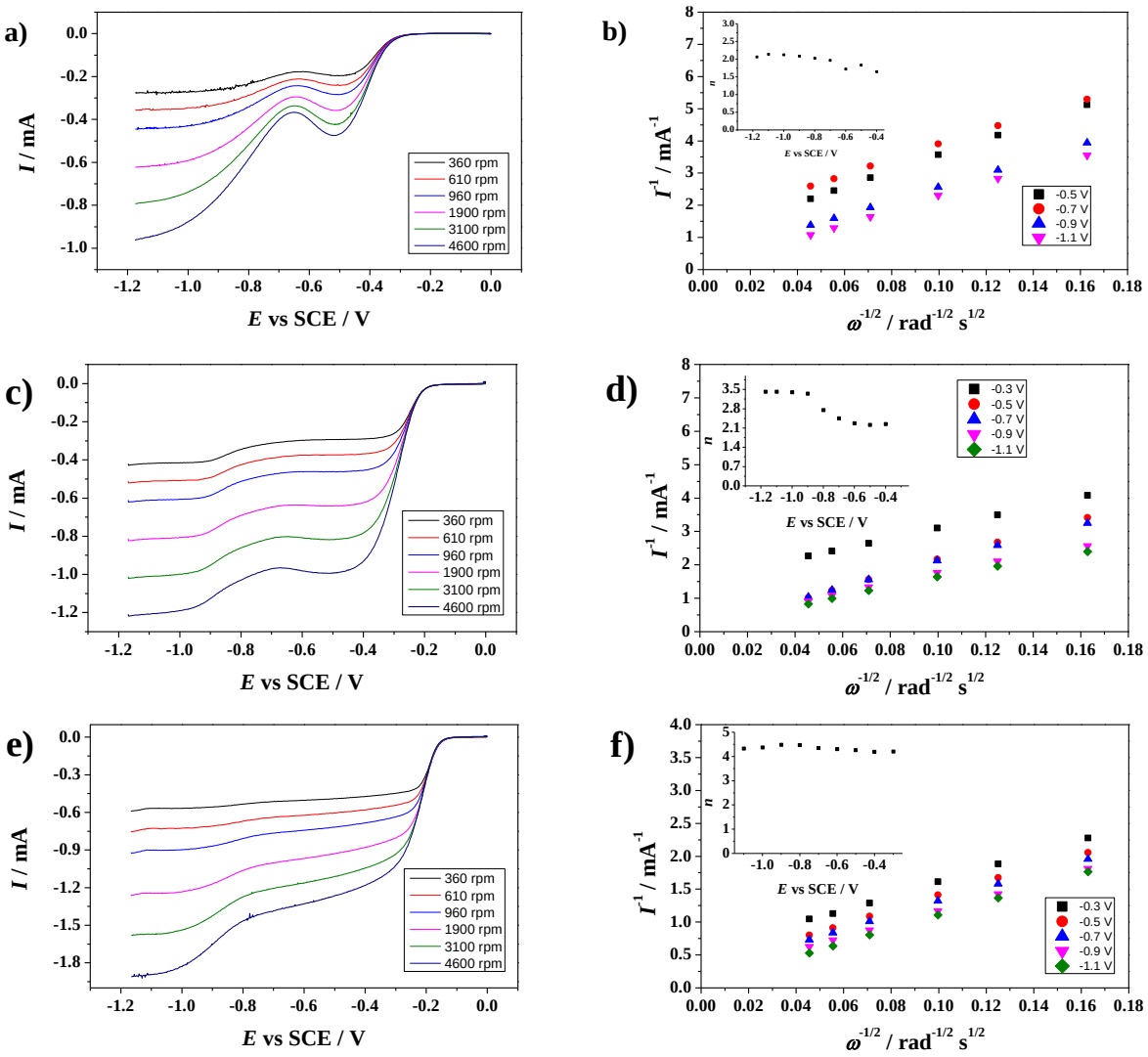

Figure 7. RDE voltammetry curves recorded at different rotation rates and Koutecky-Levich plots of (a, b) bare GC electrode, (c, d) GR-NW, (e, f) GR-NW-N/Fe/Co in O_2-saturated 0.1 KOH solution at a scan rate of 10 mV s^{-1}.

To determine the suitability of the GR-NW-N/Fe/Co to be employed at the air-electrode of RZAB, the OER studies were performed (Fig. 8). The OER polarisation curve was recorded in Ar-saturated 0.1 M KOH solution at 1900 rpm. To find the material's bifunctional activity (ΔE), a difference between the potential at a current density of 10 mA cm^{-2} for OER and half-wave potential for ORR was calculated ($\Delta E = E_{j=10} - E_{1/2}$). With an electrode area of 0.2 cm^2, current density of 10 mA cm^{-2} is equivalent to a current of 2 mA. GR-NW-N/Fe/Co achieved 2 mA at 0.65 V vs SCE and possessed a $E_{1/2}$ of -0.23 V vs SCE, which results in a ΔE value of 0.88 V. The bifunctional electrochemical behaviour of commercial Pt-Ru/C catalyst in Fig. 8 was found to be very similar according to ΔE = 0.88 V value, which itself is also consistent with the previously published data for Pt-Ru/C [33].

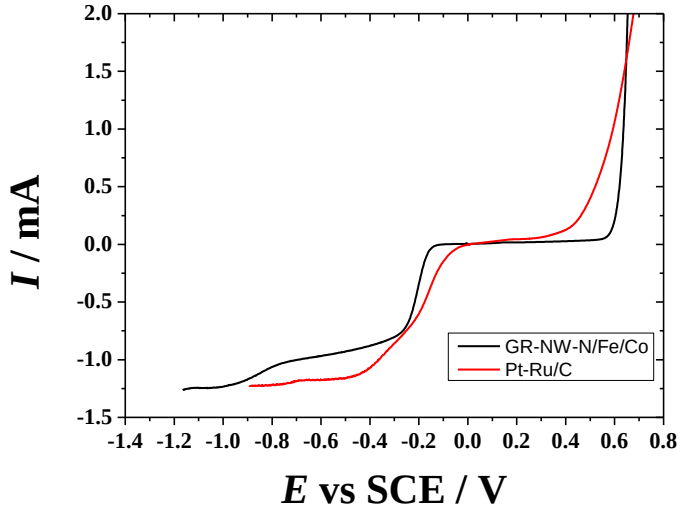

Figure 8. Combined ORR (O_2-saturated) and OER (Ar-saturated) polarization curves for Pt-Ru/C and GR-NW-N/Fe/Co catalysts at 1900 rpm in 0.1 M KOH solution.

4.3 Zinc-air battery testing

4.3.1 Primary ZAB testing results

Primary ZAB tests were performed using GR-NW-N/Fe/Co as catalyst (Fig. 9). ZAB with GR-NW-N/Fe/Co reached a maximum power density (P_{max}) of 149 mW cm^{-2}. While being able to achieve more power output than Pt-Ru/C (P_{max} = 139 mW cm^{-2}), GR-NW-N/Fe/Co had a lower open circuit voltage (OCV, 1.39 V, compared to a theoretical Zn-air voltage of 1.65 V [22]) and peak current density (191 mA cm^{-2}) than Pt-Ru/C (1.45 V and 200 mA cm^{-2}, correspondingly). The full discharge test showed that GR-NW-N/Fe/Co produces higher voltage over long time period at a constant current density of 20 mA cm^{-2} compared to Pt-Ru/C, but overall has less capacity (96 mAh vs 102 mAh). Since the Zn electrode was weighed before and after full discharge testing, specific capacity of ZAB with GR-NW-N/Fe/Co could be determined. Before discharge, the mass of the anode was measured at 1.45025 g, and after full discharge had concluded, the mass reduced to 1.39054 g. Division of discharge capacity by mass difference yields a specific capacity of 807 mAh g_{Zn}^{-1}. In the case of Pt-Ru/C, the specific capacity was determined to be 695 mAh g_{Zn}^{-1}. The gathered data indicates that GR-NW-N/Fe/Co is a better choice for primary ZAB application. GR-NW-N/Fe/Co containing ZAB can maintain higher voltage during continuous discharge and a greater maximum power output, while also possessing a higher specific capacity. However, GR-NW-N/Fe/Co-based ZAB shows lower capacity in mAh scale compared to Pt-Ru/C,

then using the mWh for capacity determination would show less difference between these two ZAB setups as the higher cell voltage of GR-NW-N/Fe/Co would also be considered.

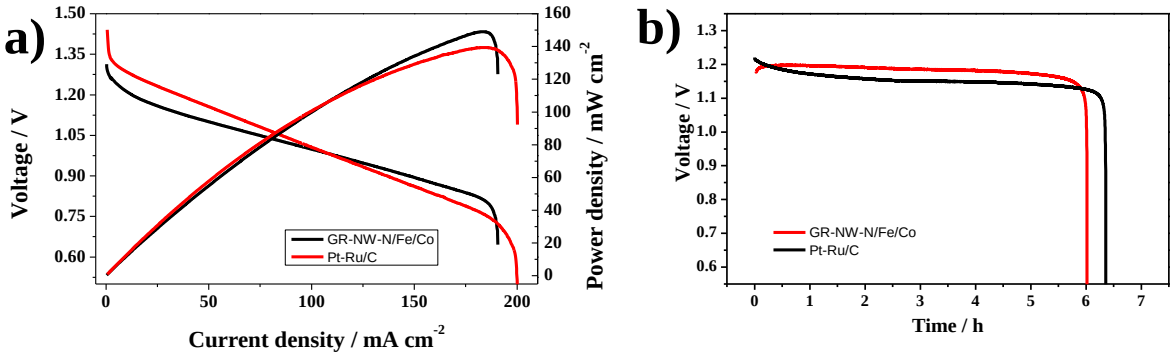

Figure 9. Primary zinc-air battery polarisation and power density curves, (b) measured voltage over time for continuous discharge at 16 mA (20 mA cm^{-2}) for Pt-Ru/C (loading 1 mg cm^{-2}) and GR-NW-N/Fe/Co (loading 2 mg cm^{-2}) air cathode catalysts.

4.3.2 Rechargeable ZAB testing

Galvanostatic charge-discharge cycling (Fig. 10) shows that on average, GR-NW-N/Fe/Co RZAB has a cycling life nearly three times as long as Pt-Ru/C RZAB, with 4 sets of cycling lasting 91 h and 32 h, correspondingly. Between the cycling runs, the mechanical recharge (i.e. reconditioning) of ZAB was performed by replacing the Zn-foil and electrolyte according to published procedure [34]. While GR-NW-N/Fe/Co possesses a longer cycling life, it is clearly visible that its charge-discharge voltage gap slightly increases over the course of each cycling run. Unlike Pt-Ru/C, which mostly stays at a static performance, but degrades rapidly at the end of each cycling run, GR-NW-N/Fe/Co air-cathode RZAB gradually loses performance throughout its lifetime until it becomes unable to function due to the formation of ZnO on the Zn electrode surface during discharging [33].

In the case of Pt-Ru/C catalyst, the irreversible loss of discharge voltage is observed at 32 h, which cannot be reversed using mechanical recharge. The ZAB with GR-NW-N/Fe/Co is successfully reconditioned after every cycling run and was only stopped as ca. 3 times longer lifetime compared to Pt-Ru/C was achieved. This indicates that GR-NW-N/Fe/Co material is much better suited for RZAB application, as it has a significantly longer cycle life, and catalyst degradation is negligibly small.

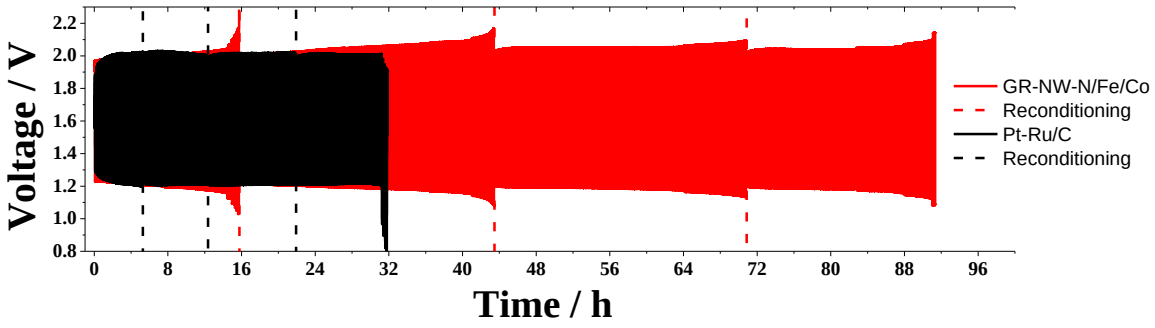

Figure 10. Galvanostatic charge-discharge cycling curves for RZAB with Pt-Ru/C and GR-NW-N/Fe/Co catalysts recorded using 10 min charge-discharge cycles at 5 mA cm^{-2}.

Table 4 presents a comparison between the catalysts investigated in this work, and materials reported in the literature. GR-NW-N/Fe/Co air-electrode catalyst performs on par with others. While possessing the highest specific capacity of all compared materials, and producing a rather strong power output, it performs slightly lower in other metrics. The GR-NW-N/Fe/Co air-electrode setup clearly outperforms Pt-Ru/C according to the P_{max} value and RZAB lifetime, but at the same time it is inferior to many other reported NPMC materials. It should be noted that in addition to the bifunctional activity of air-electrode catalyst, the specifics of the ZAB setup (e.g. air-electrode area and zinc electrode area) play a crucial role in the cell performance [41]. For example, the Co_3O_4/Fe_2O_3NAs@CNFs catalyst reported by Sun. et al. [25], exhibits the highest P_{max} in Table 4, while the ΔE is rather high compared to the others. Moreover, the P_{max} obtained for Pt/C+RuO_2 in the same work for comparison is 175 mW cm^{-2} [25] outperforming Pt-Ru/C herein and almost all the NPMCs reported in Table 4. Therefore, it is important to consider also the specifics of each ZAB setup compared to the consideration of only the air-electrode catalyst performance. In conclusion, the high specific capacity and power output make GR-NW-N/Fe/Co a good catalyst material for primary ZAB air-electrode application. Also, the remarkably higher life-time in RZAB compared to the commercial Pt-Ru/C makes the use of GR-NW-N/Fe/Co material very appealing for the secondary battery air-electrode.

Table 4. ORR, OER and RZAB performances of TM-based NPMCs.

Catalyst	$E_{1/2}$, **V**	$E_{j=10}$, **V**	ΔE, **V**	**OCV, V**	P_{max}, **mW cm^{-2}**	**Specific capacity, mAh g$_{Zn}^{-1}$**	**Stability, time@j (mA cm^{-2})**	**Ref.**
Pt-Ru/C	-0.20	0.68	0.88	1.45	139	695	32 h@5 (4 runs)	This work
GR-NW-N/Fe/Co	-0.23	0.65	0.88	1.39	149	807	91 h@5 (4 runs)	This work
FeNiN-MWCNT	-0.14*	0.58*	0.72	1.45	84.5		48 h@1	[23]
V_o-CoFe/$CoFe_2O_4$@NC	-0.15*	0.58*	0.73	1.53	138.5	774.8	45 h@10	[24]
Co_3O_4/Fe_2O_3 NAs@CNFs	-0.21*	0.59*	0.80	1.53	246		40 h@10	[25]
FeCo@NC	-0.15*	0.50*	0.66	1.44	160.1	741.5	70 h@10	[28]
CoFe-LDH@FeCo NPs-N-CNTs	-0.12*	0.56*	0.68	1.51	116	799	100 h@10	[27]
H-Co@FeCo/N/C	-0.10*	0.60*	0.70	1.45	125.2		200 h@10	[10]
CoFe@NC/NCHNSs-700	-0.09*	0.51*	0.60	1.49	184	774.1	50 h@5	[26]

*Values converted to vs SCE using equation E(vs SCE) = E(vs RHE) - 0.241 - 0.059pH [33].

SUMMARY

The electrochemical investigation of electrocatalytic oxygen reduction and oxygen evolution reactions was performed using CV and RDE methods on graphene-coated Al_2O_3 nanowires (GR-NW) modified with dicyandiamide, $FeCl_3$, and $Co(CH_3COO)_2$. GR-NW material was functionalised via high-temperature pyrolysis in an inert atmosphere. Study of primary and secondary ZAB performance was done with an in-house built ZAB cell setup.

Composition and morphology of the catalyst was evaluated by SEM-EDX, XPS, and Raman spectroscopy, indicating successful functionalization of material with minimal degradation of previously present sp^2-hybridization, as well as formation of Fe/Co alloy MNPs. XPS analysis detected doped nitrogen and M-N_x species, which facilitate the ORR activity, as well as transition metal oxides, which promote the OER process.

Electrochemical studies in 0.1 M KOH solution showed far superior ORR performance of N-, Fe-, and Co co-doped GR-NW catalyst compared to the materials with fewer dopants, with ORR exclusively proceeding the $4e^-$ pathway, and a $E_{1/2}$ value of -0.23 V (vs SCE). A further OER study was performed to evaluate the material's bifunctionality, and determined a ΔE value of 0.88 V (value calculated using iR drop correction of ORR/OER voltammetry curves), identical to that of commercial Pt-Ru/C catalyst.

Primary ZAB performance of the catalyst was evaluated by measuring maximum power output and specific capacity of the ZAB, with both values (149 mW cm^{-2} and 807 mAh g_{Zn}^{-1}) exceeding those of commercial Pt-Ru/C (139 mW cm^{-2} and 695 mAh g_{Zn}^{-1}). Secondary ZAB performance was evaluated by repetitive charge-discharge cycling until failure due to the formation of a ZnO layer, after which mechanical recharge was performed. The studied NPMC air-electrode material lasted for a total of 91 hours with 3 recharges, compared to Pt-Ru/C only lasting 32 hours with 3 recharges.

To summarize, based on the results obtained from physical and electrochemical characterisations, graphene coated Al_2O_3 nanowire co-doped with N, Fe and Co would be an appealing option as an air-electrode catalyst for both primary and rechargeable ZABs.

REFERENCES

[1] A. K. Ipadeola, A. B. Haruna, L. Gaolatlhe, A. K. Lebechi, J. Meng, Q. Pang, K. Eid, A. M. Abdullah, K. I. Ozoemena, Efforts at Enhancing Bifunctional Electrocatalysis and Related Events for Rechargeable Zinc-Air Batteries, ChemElectroChem 8 (2021) 3998-4018. https://doi.org/10.1002/celc.202100574.

[2] Y. Kumar, M. Mooste, K. Tammeveski, Recent progress of transition metal-based bifunctional electrocatalysts for rechargeable zinc-air battery application, Curr. Opin. Electrochem. 38 (2023) 101229. https://doi.org/10.1016/j.coelec.2023.101229.

[3] A. Sarapuu, E. Kibena-Põldsepp, M. Borghei, K. Tammeveski, Electrocatalysis of oxygen reduction on heteroatom-doped nanocarbons and transition metal–nitrogen–carbon catalysts for alkaline membrane fuel cells, J. Mater. Chem. A 6 (2018) 776–804. https://doi.org/10.1039/C7TA08690C.

[4] M.M. Hossen, S. Hasan, R. I. Sardar, J. b. Haider, Mottakin, K. Tammeveski, P. Atanassov, State-of-the-art and developmental trends in platinum group metal-free cathode catalyst for anion exchange membrane fuel cell (AEMFC), Appl. Catal. B: Environ. 325 (2023) 121733. https://doi.org/10.1016/j.apcatb.2022.121733.

[5] S. Hussain, N. Kongi, A. Treshchalov, T. Kahro, M. Rähn, M. Merisalu, A. Tamm, V. Sammelselg, K. Tammeveski, Enhanced oxygen reduction reaction activity and durability of Pt nanoparticles deposited on graphene-coated alumina nanofibres, Nanoscale Adv. 3 (2021) 2261-2268. https://doi.org/10.1039/D1NA00007A.

[6] D. Stock, S. Dongmo, J. Janek, D. Schröder, Benchmarking Anode Concepts: The Future of Electrically Rechargeable Zinc–Air Batteries, ACS Energy Lett. 4 (2019) 1287-1300. https://doi.org/10.1021/acsenergylett.9b00510.

[7] K. W. Leong, Y. Wang, M. Ni, W. Pan, S. Luo, D. Y. C. Leung, Rechargeable Zn-air batteries: Recent trends and future perspectives, Renew. Sust. Energ. Rev. 154 (2022) 111771. https://doi.org/10.1016/j.rser.2021.111771.

[8] J. Fu, Z. P. Cano, M. G. Park, A. Yu, M. Fowler, Z. Chen, Electrically Rechargeable Zinc–Air Batteries: Progress, Challenges, and Perspectives, Adv. Mater. 29 (2017) 1604685. https://doi.org/10.1002/adma.201604685.

[9] J. Sun, N. Wang, Z. Qiu, L. Xing, L. Du, Recent Progress of Non-Noble Metal Catalysts for Oxygen Electrode in Zn-Air Batteries: A Mini Review, Catal. 8 (2022) 843. https://doi.org/10.3390/catal12080843

[10] Y. Wu, X. Wu, T. Tu, P. Zhang, J. Li, Y. Zhou, L. Huang, S. Sun, Controlled synthesis of FeN_x-CoN_x dual active sites interfaced with metallic Co nanoparticles as bifunctional oxygen electrocatalysts for rechargeable Zn-air batteries, Appl. Catal. B: Environ. 278 (2020) 119259. https://doi.org/10.1016/j.apcatb.2020.119259.

[11] J. K. Nørskov, J. Rossmeisl, A. Logadottir, L. Lindqvist, J. R. Kitchin, T. Bligaard, H. Jonsson, Origin of the Overpotential for Oxygen Reduction at a Fuel-Cell Cathode, J. Phys. Chem. B 108 (2004) 17886-17892. https://doi.org/10.1021/jp047349j.

[12] G. Yusibova, J.-M. Assafrei, K. Ping, J. Aruväli, P. Paiste, M. Käärik, J. Leis, H.-M. Piirsoo, A. Tamm, A. Kikas, V. Kisand, P. Starkov, N. Kongi, Bimetallic metal-

organic-framework-derived porous cobalt manganese oxide bifunctional oxygen electrocatalyst, J. Electroanal. Chem. 930 (2023) 117161. https://doi.org/10.1016/j.jelechem.2023.117161.

[13] R. Liu, D. Wu, X. Feng, K. Müllen, Nitrogen-doped ordered mesoporous graphitic arrays with high electrocatalytic activity for oxygen reduction, Angew. Chem. Int. Ed. Engl. 49 (2010) 2565-2569. https://doi.org/10.1002/anie.200907289.

[14] H. W. Liang, X. Zhuang, S. Brüller, X. Feng, K. Müllen, Hierarchically porous carbons with optimized nitrogen doping as highly active electrocatalysts for oxygen reduction, Nat. Commun. 5 (2014) 4973. https://doi.org/10.1038/ncomms5973.

[15] R. Jasinski, A New Fuel Cell Cathode Catalyst, Nature 201 (1964) 1212-1213. https://doi.org/10.1038/2011212a0.

[16] V. S. Bagotzky, M. R. Tarasevich, K. A. Radyushkina, O. A. Levina, S. I. Andrusyova, Electrocatalysis of the oxygen reduction process on metal chelates in acid electrolyte, J. Power Sources 2 (1978) 233-240. https://doi.org/10.1016/0378-7753(78)85014-9.

[17] S. Gupta, D. Tryk, I. Bae, W. Aldred, E. Yeager, Heat-treated polyacrylonitrile-based catalysts for oxygen electroreduction, J. Appl. Electrochem. 19 (1989) 19-27. https://doi.org/10.1007/BF01039385.

[18] J. Lilloja, M. Mooste, E. Kibena-Põldsepp, A. Sarapuu, A. Kikas, V. Kisand, M. Käärik, J. Kozlova, A. Treshchalov, P. Paiste, J. Aruväli, J. Leis, A. Tamm, S. Holdcroft, K. Tammeveski, Cobalt-, iron- and nitrogen-containing ordered mesoporous carbon-based catalysts for anion-exchange membrane fuel cell cathode, Electrochim. Acta 439 (2023) 141676. https://doi.org/10.1016/j.electacta.2022.141676.

[19] S. Juvanen, A. Sarapuu, M. Mooste, M. Käärik, U. Mäeorg, A. Kikas, V. Kisand, J. Kozlova, A. Treshchalov, J. Aruväli, J. Leis, A. Tamm, K. Tammeveski, Electroreduction of oxygen on iron- and cobalt-containing nitrogen-doped carbon catalysts prepared from the rapeseed press cake, J. Electroanal. Chem. 920 (2022) 116599. https://doi.org/10.1016/j.jelechem.2022.116599.

[20] A. Sokka, M. Mooste, M. Käärik, V. Gudkova, J. Kozlova, A. Kikas, V. Kisand, A.Treshchalov, A. Tamm, P. Paiste, J. Aruväli, J. Leis, A. Krumme, S. Holdcroft, S. Cavaliere, F. Jaouen, K. Tammeveski, Iron and cobalt containing electrospun carbon nanofibre-based cathode catalysts for anion exchange membrane fuel cell, Int. J. Hydrogen Energy 46 (2021) 31275-31287. https://doi.org/10.1016/j.ijhydene.2021.07.025.

[21] Y. Kumar, E. Kibena-Põldsepp, J. Kozlova, M. Rähn, A. Treshchalov, A. Kikas, V. Kisand, J. Aruväli, A. Tamm, J. C. Douglin, S. J. Folkman, I. Gelmetti, F. A. Garcés-Pineda, J. R. Galán-Mascarós, D. R. Dekel, K. Tammeveski, Bifunctional Oxygen Electrocatalysis on Mixed Metal Phthalocyanine-Modified Carbon Nanotubes Prepared via Pyrolysis, ACS Appl. Mater. Interfaces 13 (2021) 41507-41516. https://doi.org/10.1021/acsami.1c06737.

[22] L. S. Bezerra, M. Mooste, G. V. Fortunat, E. S. F. Cardoso, M. R. V. Lanza, K. Tammeveski, G. Maia, Tuning $NiCo_2O_4$ bifunctionality with nitrogen-doped graphene nanoribbons in oxygen electrocatalysis for zinc-air battery application, J. Electroanal. Chem. 928 (2023) 117000. https://doi.org/10.1016/j.jelechem.2022.117000.

[23] Y. Kumar, E. Kibena-Põldsepp, M. Mooste, J. Kozlova, A. Kikas, J. Aruväli, M. Käärik, V. Kisand, J. Leis, A. Tamm, S. Holdcroft, J. H. Zagal, K. Tammeveski, Iron and Nickel Phthalocyanine-Modified Nanocarbon Materials as Cathode Catalysts for Anion-Exchange Membrane Fuel Cells and Zinc-Air Batteries, ChemElectroChem 9, e202200717. https://doi.org/10.1002/celc.202200717.

[24] Y. Go, K. Min, H. An, K. Kim, S. Eun Shim, S.-H. Baeck, Oxygen-vacancy-rich CoFe/$CoFe_2O_4$ embedded in N-doped hollow carbon spheres as a highly efficient bifunctional electrocatalyst for Zn–air batteries, Chem. Eng. J. 448 (2022) 137665. https://doi.org/10.1016/j.cej.2022.137665.

[25] L. Sun, Y. Qin, L. Fu, Y. Di, K. Hu, H. Li, L. Li, W. Zhang, A self-supported bifunctional air cathode composed of Co_3O_4/Fe_2O_3 nanoparticles embedded in nanosheet arrays grafted onto carbon nanofibers for secondary zinc-air batteries, J. Alloys Compd. 921 (2022) 166128. https://doi.org/10.1016/j.jallcom.2022.166128.

[26] S. Wang, H. Wang, C. Huang, P. Ye, X. Luo, J. Ning, Y. Zhong, Y. Hu, Trifunctional electrocatalyst of N-doped graphitic carbon nanosheets encapsulated with CoFe alloy nanocrystals: The key roles of bimetal components and high-content graphitic-N, Appl. Catal. B: Environ. 298 (2021) 120512. https://doi.org/10.1016/j.apcatb.2021.120512.

[27] T. Zhang, J. Bian, Y. Zhu, C. Sun, FeCo Nanoparticles Encapsulated in N-Doped Carbon Nanotubes Coupled with Layered Double (Co, Fe) Hydroxide as an Efficient Bifunctional Catalyst for Rechargeable Zinc–Air Batteries, Small 17 (2021) 2103737. https://doi.org/10.1002/smll.202103737.

[28] Z. Wang, X. Zhou, H. Jin, D. Chen, J. Zhu, R. Hempelmann, L. Chen, S. Mu, Ionic liquid-derived FeCo alloys encapsulated in nitrogen-doped carbon framework as advanced bifunctional catalysts for rechargeable Zn-air batteries, J. Alloys Compd. 908 (2022) 164565. https://doi.org/10.1016/j.jallcom.2022.164565.

[29] Y. Kumar, E. Kibena-Põldsepp, J. Kozlova, A. Kikas, M. Käärik, J. Aruväli, V. Kisand, J. Leis, A. Tamm, K. Tammeveski, Bimetal Phthalocyanine-Modified Carbon Nanotube-Based Bifunctional Catalysts for Zinc-Air Batteries, ChemElectroChem 8 (2021) 2662-2670. https://doi.org/10.1002/celc.202100498.

[30] R. Ivanov, Chemical Vapour Deposition of Graphene Coating onto Ceramic Nanofibers Substrates and Applications Thereof, Tallinn University of Technology, Tallinn, 2017.

[31] S. Ratso, I. Kruusenberg, A. Sarapuu, M. Kook, P. Rauwel, R. Saar, J. Aruväli, K. Tammeveski, Electrocatalysis of oxygen reduction on iron- and cobalt-containing nitrogen-doped carbon nanotubes in acid media, Electrochim. Acta 218 (2016) 303-310. https://doi.org/10.1016/j.electacta.2016.09.119.

[32] M. Mooste, E. Kibena-Põldsepp, V. Vassiljeva, M. Merisalu, M. Kook, A. Treshchalov, V. Kisand, M. Uibu, A. Krumme, V. Sammelselg, K. Tammeveski, Electrocatalysts for oxygen reduction reaction based on electrospun polyacrylonitrile, styrene–acrylonitrile copolymer and carbon nanotube composite fibres, J. Mater. Sci. 54 (2019) 11618-11634. https://doi.org/10.1007/s10853-019-03725-z.

[33] P. Moni, M. Mooste, K. Tammeveski, K. Rezwan, M. Wilhelm, One-dimensional polymer-derived ceramic nanowires with electrocatalytically active metallic silicide

tips as cathode catalysts for Zn–air batteries, RSC Adv. 11 (2021) 39707-39717. https://doi.org/10.1039/D1RA05688C.

[34] K. Muuli, X. Lyu, M. Mooste, M. Kääri, B. Zulevi, J. Leis, H. Yu, D. A. Cullen, A. Serov, K. Tammeveski, Outstanding platinum group metal-free bifunctional catalysts for rechargeable zinc-air batteries, Electrochim. Acta 446 (2023) 142126. https://doi.org/10.1016/j.electacta.2023.142126.

[35] K. Kim, K. Min, Y. Go, Y. Lee, S. E. Shim, D. Lim, S.-H. Baeck, FeCo alloy nanoparticles embedded in N-doped carbon supported on highly defective ketjenblack as effective bifunctional electrocatalysts for rechargeable Zn–air batteries, Appl. Catal. B: Environ. 315 (2022) 121501. https://doi.org/10.1016/j.apcatb.2022.121501.

[36] M. Peña-Álvarez, E. d. Corro, F. Langa, V. G. Baonza, M. Taravillo, Morphological changes in carbon nanohorns under stress: a combined Raman spectroscopy and TEM study, RSC Adv. 6 (2016) 49543-49550. https://doi.org/10.1039/C5RA27162B.

[37] A. R. Barron, P. M. V. Raja, Raman Spectroscopy, in: Physical Methods in Chemistry and Nano Science, LibreTexts, Houston, 2023, pp. 297-308.

[38] M. Mooste, E. Kibena-Põldsepp, L. Matisen, K. Tammeveski, Oxygen Reduction on Anthraquinone Diazonium Compound Derivatised Multi-walled Carbon Nanotube and Graphene Based Electrodes, Electroanal. 29 (2017) 548-558. https://doi.org/10.1002/elan.201600451.

[39] A. J. Bard, L. R. Faulkner, Electrochemical Methods: Fundamentals and Applications, second ed., Wiley, New York, 2001.

[40] M. Mooste, E. Kibena-Põldsepp, L. Matisen, M. Merisalu, M. Kook, V. Kisand, V. Vassiljeva, A. Krumme, V. Sammelselg, K. Tammeveski, Oxygen Reduction on Catalysts Prepared by Pyrolysis of Electrospun Styrene–Acrylonitrile Copolymer and Multi-walled Carbon Nanotube Composite Fibres, Catal. Lett. 148 (2018) 1815-1826. https://doi.org/10.1007/s10562-018-2392-6.

[41] Z. Pei, H. Li, Y. Huang, Q. Xue, Y. Huang, M. Zhu, Z. Wang, C. Zhi, Texturing in situ: N,S-enriched hierarchically porous carbon as a highly active reversible oxygen electrocatalyst, Energy Environ. Sci. 10 (2017) 742-749. https://doi.org/10.1039/C6EE03265F.

ACKNOWLEDGEMENTS

I would like to express my sincere gratitude, appreciation and respect to my supervisor, Dr. Marek Mooste, for his patience and willingness to help, for taking the time to share his knowledge with me and providing continuous guidance and advice throughout this research and beyond. I am thankful for the experience I have received while working under his supervision.

I wish to thank Prof. Kaido Tammeveski for giving me an opportunity to conduct this research and his support throughout.

I wish to express my appreciation to the research staff at the University of Tartu Institute of Physics for their contribution to this thesis, and to the research staff at the University of Tatu Institute of Chemistry for their continuous support and willingness to help with this work.

Appendix

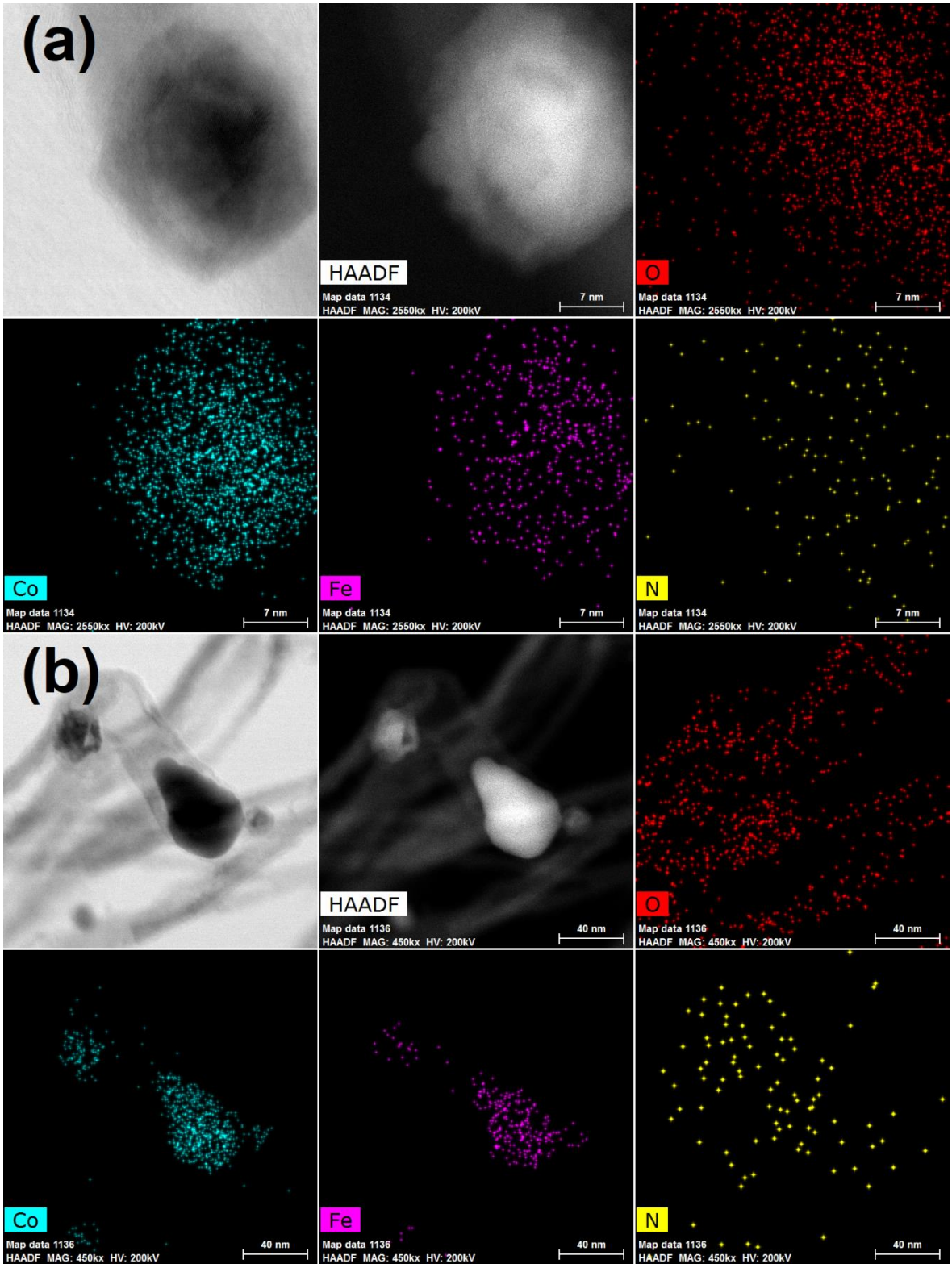

Figure S1. STEM images and elemental maps of GR-NW-N/Fe/Co.

NON-EXCLUSIVE LICENCE TO REPRODUCE THESIS AND MAKE THESIS PUBLIC

I, PAVELS KAPITULSKIS,

1. grant the University of Tartu a free permit (non-exclusive licence) to:

reproduce, for the purpose of preservation, including for adding to the DSpace digital archives until the expiry of the term of copyright, my thesis

Cobalt, iron, and nitrogen co-doped graphene coated ceramic nanowire-based bifunctional oxygen electrocatalyst for Zn-air battery,

supervised by Kaido Tammeveski and Marek Mooste,

2. I grant the University of Tartu the permit to make the thesis specified in point 1 available to the public via the web environment of the University of Tartu, including via the DSpace digital archives, under the Creative Commons licence CC BY NC ND 4.0, which allows, by giving appropriate credit to the author, to reproduce, distribute the work and communicate it to the public, and prohibits the creation of derivative works and any commercial use of the work from ***20/06/2024*** until the expiry of the term of copyright,

3. I am aware that the author retains the rights specified in points 1 and 2.

4. I confirm that granting the non-exclusive licence does not infringe other persons' intellectual property rights or rights arising from the personal data protection legislation.

Pavels Kapitulskis

14/05/2023